Supplementary Materials for

Atomic dynamics of electrified solid-liquid interfaces in liquid cell TEM

Qiubo Zhang *et al*.

Corresponding author: hmzheng@lbl.gov

The PDF file includes:

Supplementary Notes 1-4
Supplementary Figs. 1-33
Supplementary Tables 1-2
References 1-8

Other Supplementary Materials for this manuscript include the following:

Supplementary Videos 1-9

Supplementary Note 1: Experimental design

To simulate the electroreduction of carbon dioxide by copper catalysts in electrolytes and to observe the microscopic details of solid-liquid interface evolution during the reaction, we developed a polymer electrochemical liquid cell (PLC) for transmission electron microscopy (TEM). Compared to the existing silicon nitride electrochemical liquid cell, the PLC offers several advantages: it provides high spatial resolution at the atomic-level with in situ liquid cell TEM; it allows in situ electron dispersive x-ray spectroscopy (EDS) and electron energy loss spectroscopy (EELS) characterization of intermediate states; it is compatible with acidic and alkaline environments; and it can withstand rapid cooling conditions for in situ Cryo-EM techniques. For in situ catalytic experiments, we used copper nanowires as the catalyst. They can be suspended on Pt electrodes, which enable superb high resolution imaging of the extended parts of nanowire. Our in situ electrochemical liquid cell employs a two-electrode system, charging of the electrode during the reaction can cause a deviation in potential, which cannot accurately reflect the potential applied to the electrode. To overcome this limitation, we incorporated two approaches. First, we calculated the difference between the Pt electrode and the reversible hydrogen electrode to compensate the potential deviation caused by the charging. Second, we used a larger negative bias voltage (-1.82 V vs. Pt is equivalent to -1.1V vs. RHE) in our in situ experiment and a range of bias voltages in ex situ experiments to test the structure of the activated catalyst in response to the potential deviation caused by charging. Our results demonstrated that the observed amorphization on the catalyst surfaces can occur under a wide range of applied electric potential. Thus, our in situ experiments combining with systematic ex situ control experiments allow unveiling of the phenomena intrinsic to the electrified solid-liquid interfaces during electrocatalytic reactions.

Supplementary Note 2: The observation of an amorphous interphase on the surface of copper catalysts in actual electrocatalytic reactions

During in situ TEM experiments, we observed amorphous interphase on the surface of copper under electric biasing (**Supplementary Figs. 27-29**). However, in the absence of biasing, the copper catalyst surface did not exhibit any amorphous state (**Supplementary Fig. 6**). Therefore, we deduced that the amorphous interphase on the copper surface occur during the carbon dioxide reduction reaction.

We conducted a series of control experiments, which revealed that the amorphous layer can be captured in ex situ CO_2 electroreduction experiments with careful control of experiments. Initially, we activated the Cu catalyst in an ex situ CO_2 electroreduction experiment for 0-30 minutes, then rinsed the activated Cu nanowires with water and quickly examined them using TEM. Surprisingly, we found that the surface of the activated copper was clean without visible amorphous layer, but the previously flat copper surface was now curved (**Supplementary Fig. 8**). We consider the amorphous state may have been removed from the surface during rinsing.

Then, we performed the same experiment on the Cu nanowires without water rinse, simply using filter paper to remove the electrolyte and immediately characterizing it using TEM. We found that the surface of the activated Cu nanowires had a crystalline layer of cuprous oxide instead of an amorphous layer (**Supplementary Fig. 9**). We hypothesized that the amorphous layer is unstable without protection and it spontaneously crystallizes into cuprous oxide at room temperature upon exposure to the air[1].

Lastly, we treated the activated sample with low-temperature and prevented it from being oxidized. As detailed in the methods section, we transferred the activated copper nanowire sample under biasing to liquid nitrogen, where the activated copper catalyst was shielded from oxygen by

fast freezing. Subsequently, we loaded the sample into a Gantan Cryo-transfer 915 holder for TEM characterization. During TEM imaging, we carefully control the electron beam intensity. We found under an extended high electron beam current, crystallize amorphous materials can be transformed into copper hydroxide. With reduced electron beam intensity, the amorphous interphase was observed on the crystalline Cu surface under different biased voltage conditions (-1.828 V to -1.228 V vs. Pt: see **Supplementary Figs. 10-17**). Therefore, the appearance of the amorphous layer on the surface of activated copper nanowires during CO_2 electroreduction is a real phenomenon that can occur over a large range of biases.

Supplementary Note 3: Electron beam effects

The electron beam irradiation may introduce electrostatic charging, local heating as excited states decay to phonons, ionization from radiolysis of electrolyte solution[2].

It is complicated to predict the effects of electrostatic charging on a given sample configuration because it is hard to quantify how well the Cu nanowire is electrically isolated from the TEM support or its environment. In our experimental setup, Cu nanowires are connected to Pt electrodes. It is reasonable to assume that surface charges generated solely by electron beam irradiation can be easily dissipated, resulting in a relatively minor effect on the charged surface.

Localized electron beam heating can aid structural transformations of nanocrystals, such as crystallization of amorphous structure[3] or amorphization of crystalline structure[4]. Inelastic transitions induced by incident electrons, which may include multiple scattering events, increase the local temperature when those excited states decay. However, previous reports also showed that the electron beam induced temperature rise in a liquid cell can be negligible[5,6].

For the potential impact of ionization from radiolysis of electrolyte, it may be significant on the electrochemical processes of investigation. Although it is hard to avoid completely, it can be managed and minimized by controlling the electron beam dose, using a thinner liquid cell as shown in this work.

To eliminate the electron beam effects on conclusions drawn from the in situ experiments, we conducted systematic control experiments, including ex situ experiments without electron beam, without/with an applied electric biasing, varying the electron dose, etc. For example, the impact of electron beam radiation is expected to occur regardless of an applied electric bias. However, our experiments showed that no amorphous interphase can be found without an applied electric bias (**Supplementary Fig. 6**). Therefore, we can rule out the electron beam effects as the main cause of the observed amorphization on copper surface.

We also conducted a series of control experiments under different electron beam dose. Our experiments showed that under a high electron dose with extended electron beam irradiation crystalline $Cu(OH)_2$ structure can be found in the amorphous interphase (**Supplementary Fig. 18**). The electron beam irradiation induced crystallization of amorphous structure had also been reported in the previous studies[3]. The liquid-like amorphous interphase was observed under controlled electron beam conditions.

Supplementary Note 4: Analysis of applied electric potential bias

The potential deviation in in situ experiments mainly stems from two sources: 1) by different reference electrodes, and 2) by electrode charging. In a two-electrode system, the counter electrode can serve as a pseudo reference electrode. Therefore, before applying any bias, we must convert the potential relative to the Pt electrode to the potential relative to the reversible hydrogen electrode. In the assembled in situ TEM cell, a cyclic voltammetry (CV) experiment is conducted

to evaluate the redox signature of $K_3[Fe(CN)_6]$. To calibrate the potential of the Pt counter electrode (i.e., a pseudo reference electrode), its half-wave potential (0 V vs Pt) is compared to the half-wave potential (0.1 V vs Ag/AgCl) in a bulk electrochemical cell. This comparison yields a calibration of the Pt reference electrode potential: E vs RHE = E vs Pt + 0.728 (V), assuming a constant pH of 8. Throughout the manuscript, this calibration is used to report the in situ measured potential relative to the RHE.

Following calibration of the Pt pseudo-reference electrode, the primary source of potential deviation is the surface charging of the electrode. Based on electrode polarization characteristics (i.e., cathodic potential being more negative than the equilibrium potential and anodic potential being more positive than the equilibrium potential), we infer that the actual potential applied to the copper catalyst in the in situ experiment is more positive than -1.1 V. Consequently, we conducted a series of ex situ experiments under varying electric potentials (-1.828 V to -1.228 V vs. Pt) to validate the observation of an amorphous interphase (**Supplementary Figs. 10-17**).

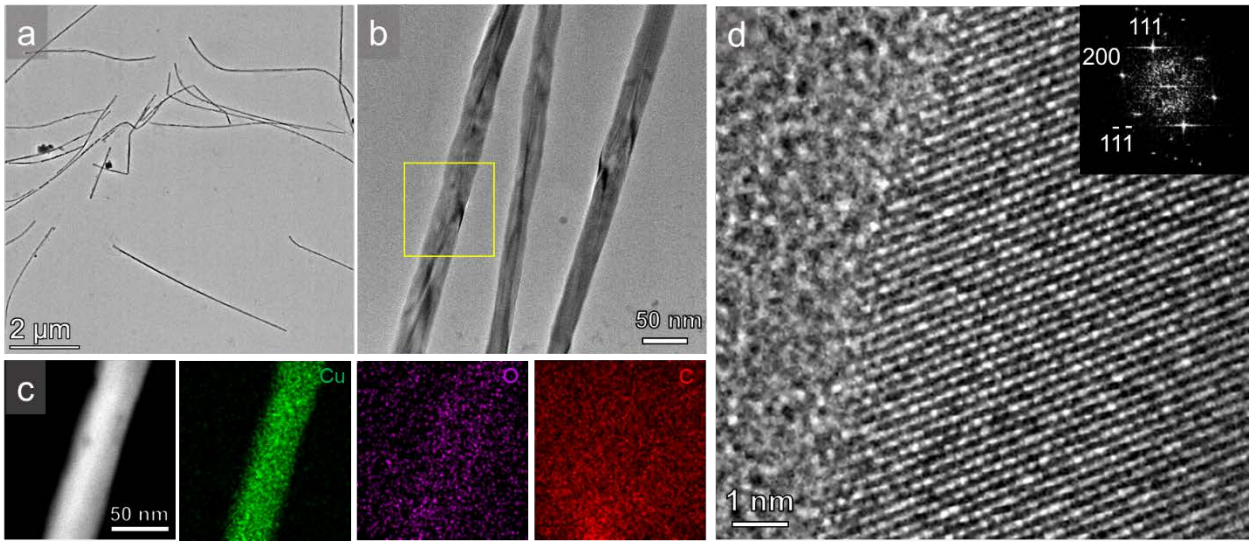

Supplementary Fig. 1 | Size and chemical element characterization of as-prepared Cu nanowires. a, Low magnification TEM image shows the size features of Cu nanowires. **b**, Low magnification TEM image of one Cu nanowire. **c**, STEM-EDX elemental mapping of Cu nanowire: HAADF image, Cu map, O map, and C map. **d**, HRTEM image and the corresponding FFT pattern of the Cu nanowire shows the single crystal structure.

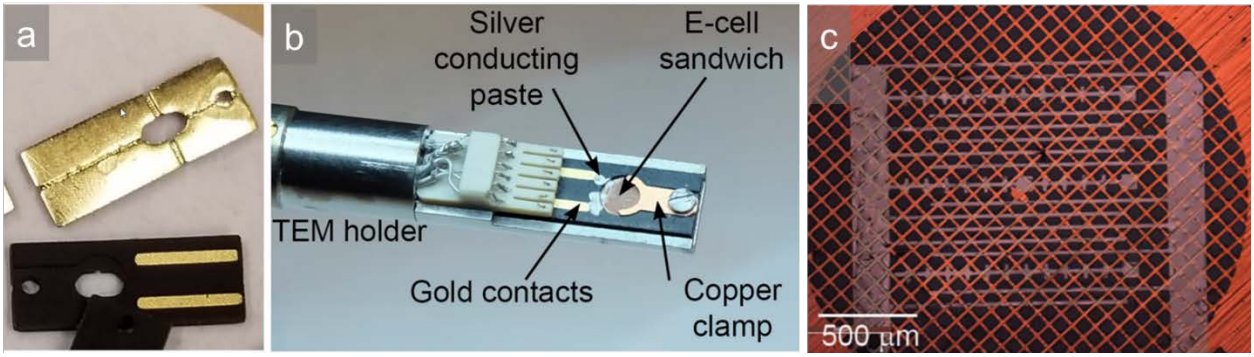

Supplementary Fig. 2 | The introduction of our homemade in situ electrochemical liquid cell system. **a**, A 3D-printed PV board is used for fixing, connecting, and anti-static for liquid cells. The gold coating on the backside is anti-static, and the two gold lines on the front are used to connect the electrodes in the liquid cell. **b**, The physical drawing of our modified electrical TEM holder shows the installation of the liquid cell. **c**, The image of an assembled liquid cell, the different patterns are used to distinguish positive and negative electrodes.

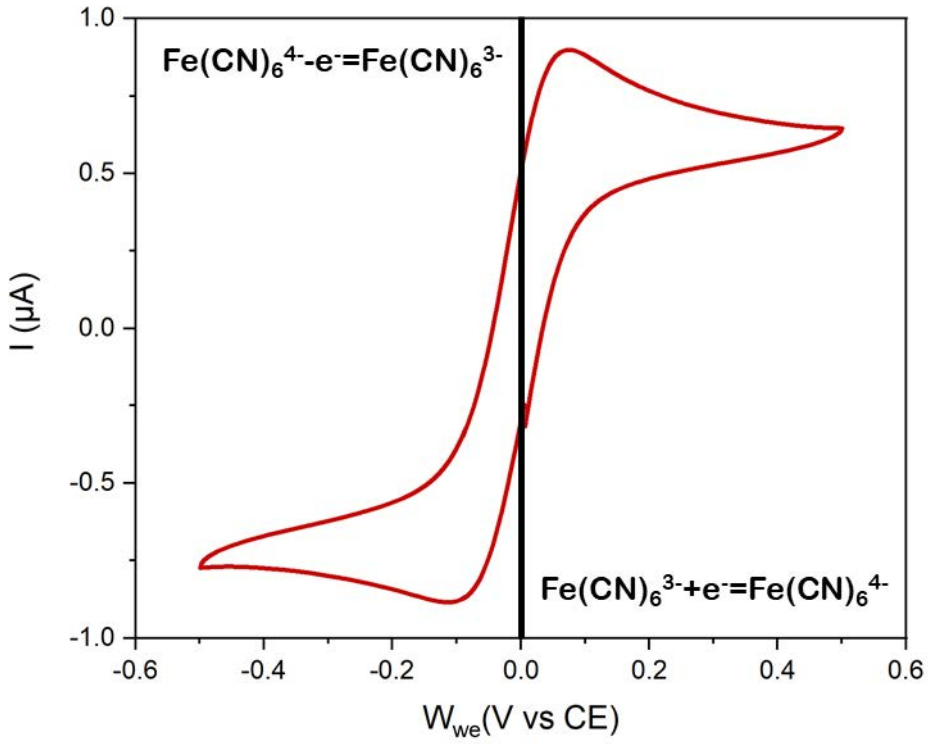

Supplementary Fig. 3 | The redox signature of $K_3[Fe(CN)_6]$ was assessed through a cyclic voltammetry (CV) experiment conducted within an in situ polymer electrochemical liquid cell. The half-wave potential depicted in the figure is at 0 V. The electrolyte used in the experiment consisted of 0.1 M $KHCO_3$ with 10 mM $K_3[Fe(CN)_6]$, while the CV was measured with a scan rate of 50 mV/s.

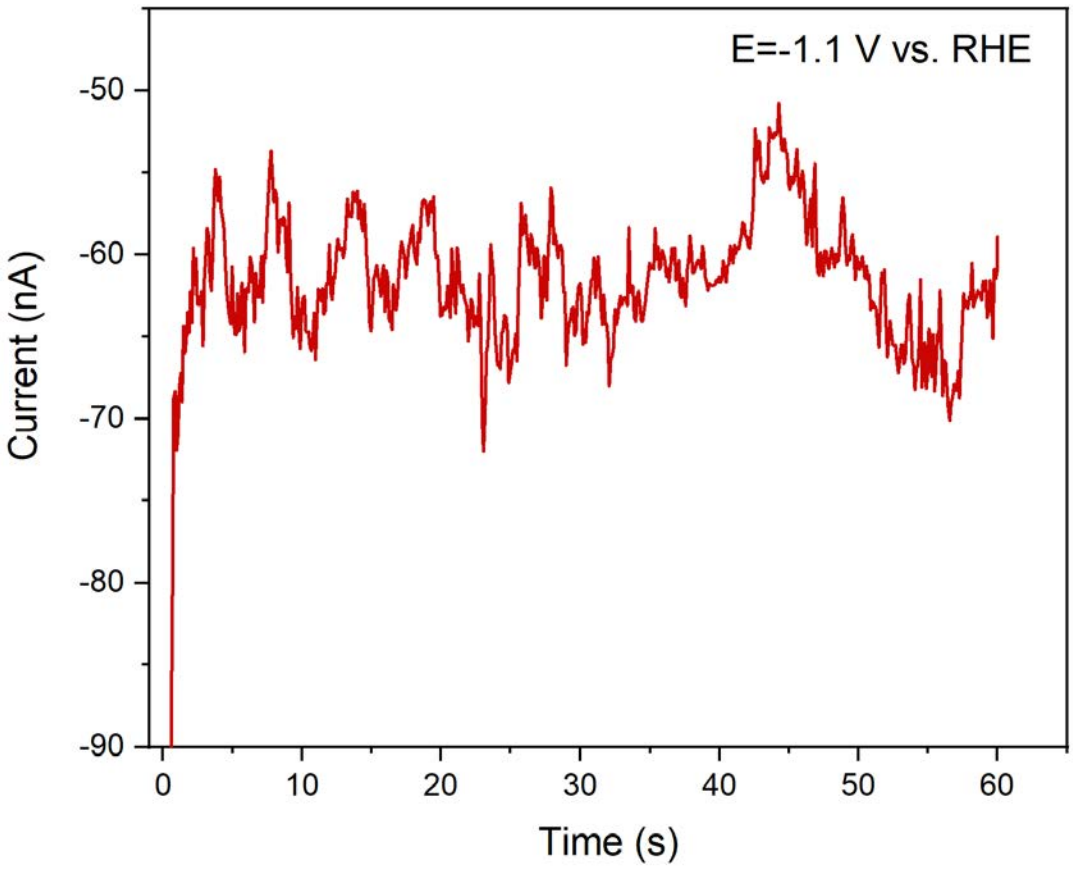

Supplementary Fig. 4 | Chronoamperometry (CA) profile of the Cu NWs at -1.828 V vs. Pt (-1.1 V vs. RHE), showing the current variations during *operando* TEM measurements. corresponding to movie S1. Beam condition is 2360 e/Å^{2}s.

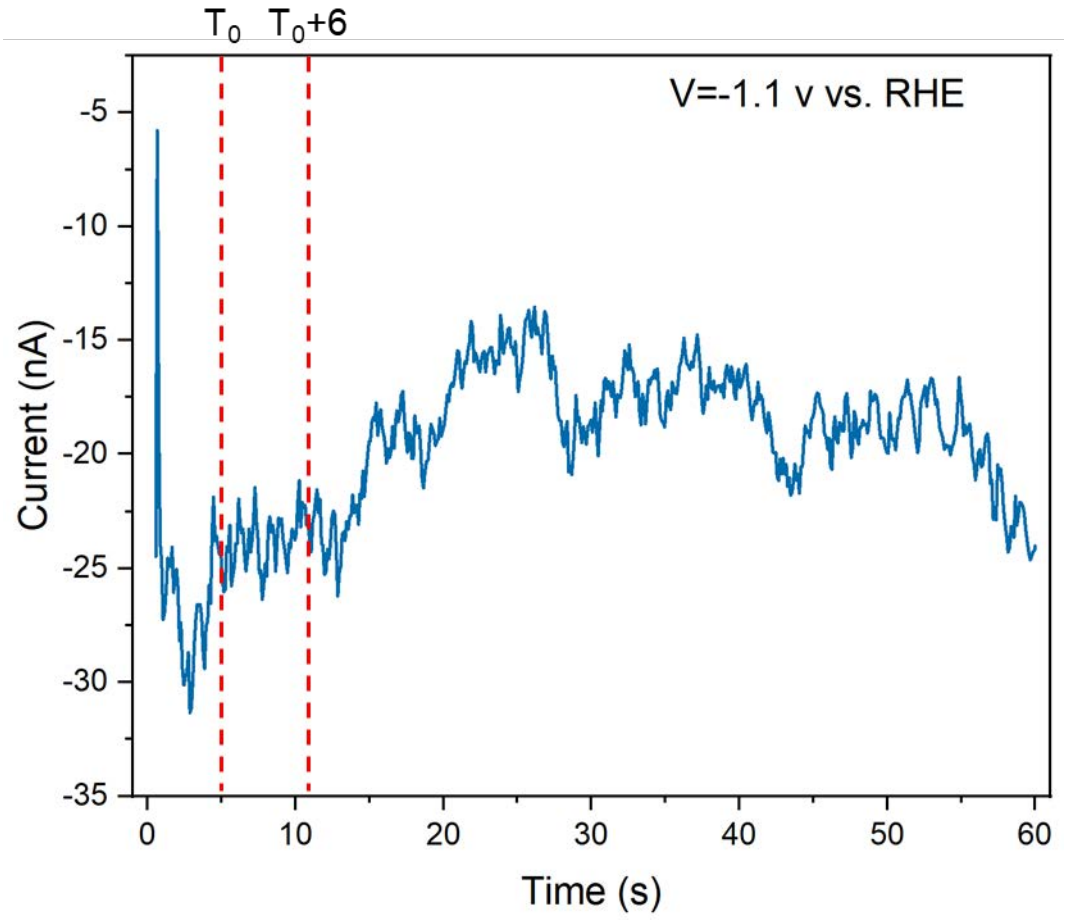

Supplementary Fig. 5 | Chronoamperometry (CA) profile of the Cu NWs at -1.828 V vs. Pt (-1.1 V vs. RHE), showing the current variation during *operando* TEM measurements, Period from T_0 toT_0+6 seconds corresponding to movie S6. After capturing Movie S6, the liquid pocket is close to dry. Beam condition is 2360 e/Å^{2}s.

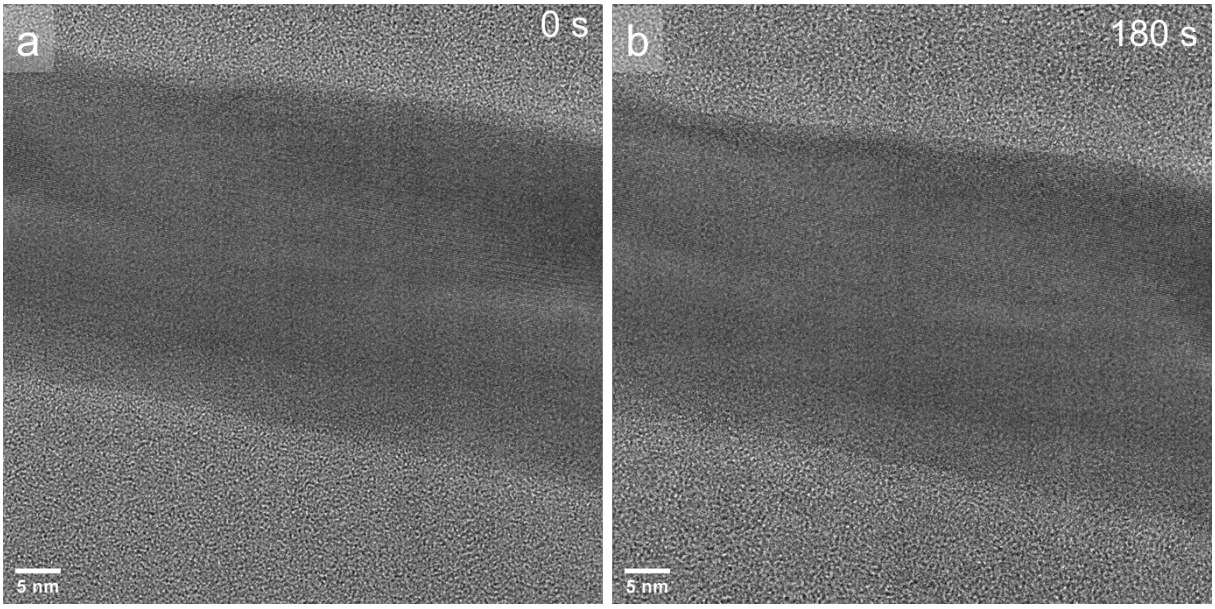

Supplementary Fig. 6 | The morphology evolution of copper nanowires under the same electron beam irradiation without electric biasing. a, HRTEM image of a Cu nanowire at the initial state. **b**, HRTEM image of a Cu nanowire after 180 seconds electron beam irradiation.

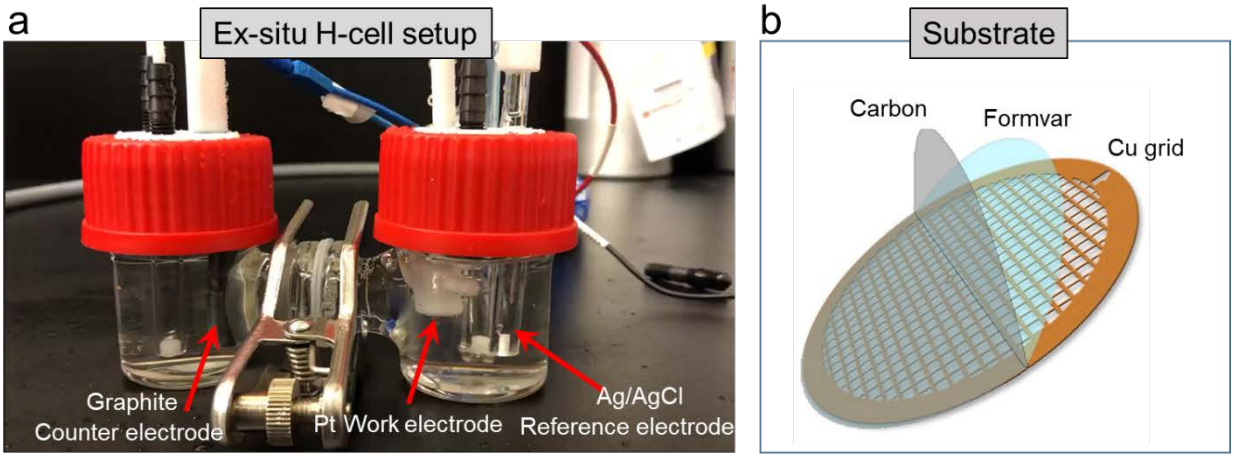

Supplementary Fig. 7 | Setup of ex situ CO_2 reduction reaction experiments. a, Image of H-cell setup for conducting CO_2 reduction reactions. **b**, Components of the substrate for supporting the catalysts.

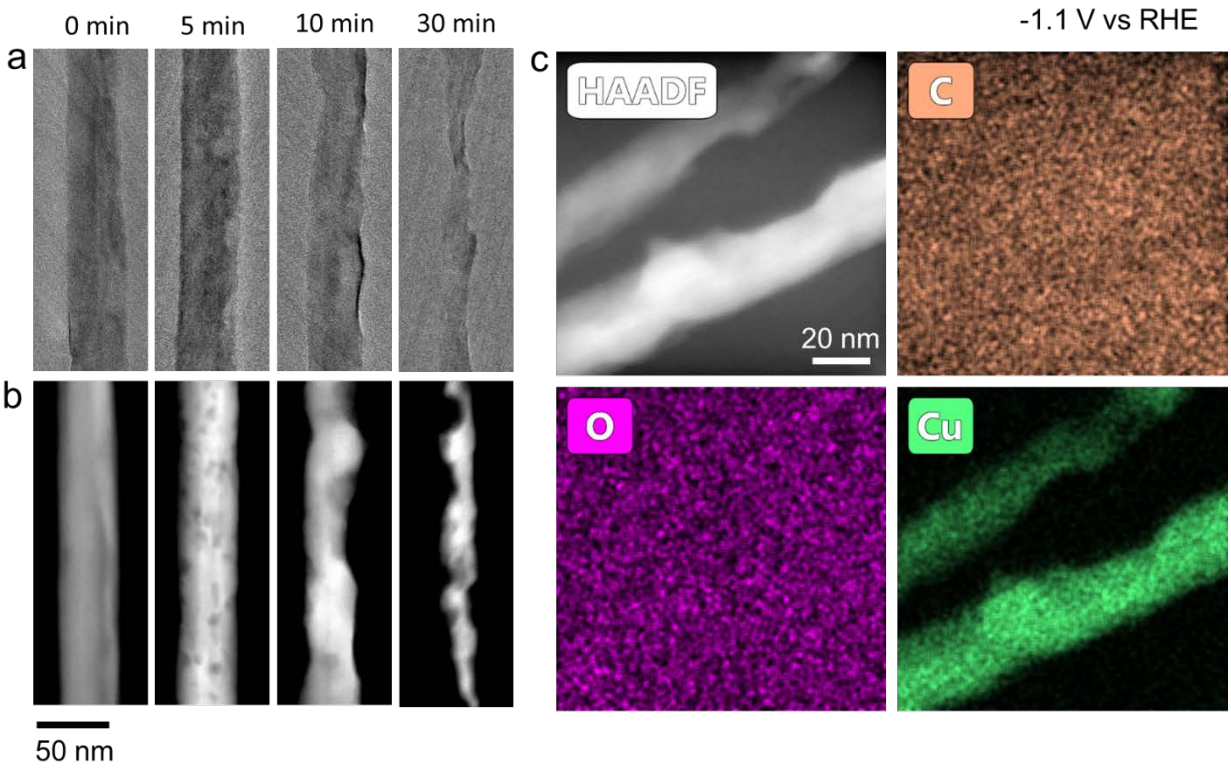

Supplementary Fig. 8 | Characterization of activated copper nanowire catalysts (after raising with water). (**a**) TEM images and (**b**) STEM images demonstrate the shape changes that occur after varying periods of activation. **c**, EDX mapping of the activated Cu nanowire.

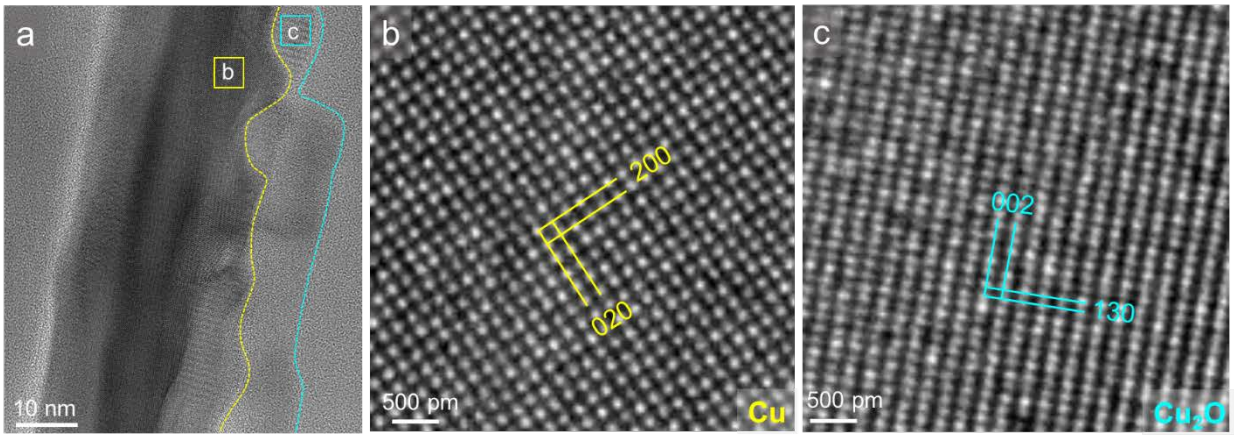

Supplementary Fig. 9 | Characterization of activated copper nanowire catalysts (After drying the electrolyte with filter paper). a, The TEM image of an activated nanowire, with yellow and blue dotted lines indicating the boundary of different phases. **b**, The HRTEM image of the yellow square region reveals that the crystal structure belongs to the FCC Cu phase. **c**, The HRTEM image of the indigo square region reveals that the crystal structure belongs to the FCC Cu_2O phase.

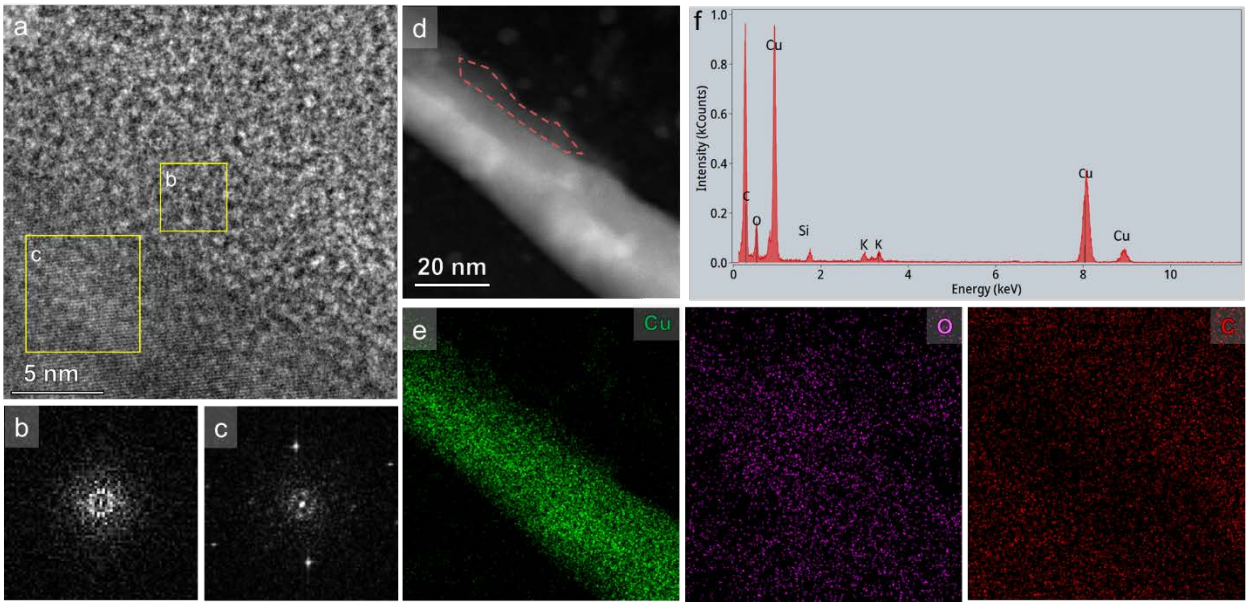

Supplementary Fig. 10 | The characterization of activated copper nanowires by cryo-TEM techniques. (Activation condition: -1.1 V VS. RHE, 30 min) a, HRTEM images of activated nanowires reveal that their structure consists of two distinct parts. **b**, The FFT of square B in Figure A indicates that it possesses an amorphous structure. **c**, The FFT of square C in (**a**) indicates that it possesses a crystal structure. **d**, HAADF image and (**e**) EDX mapping show the elemental composition. **f**, The EDX spectrum extracted from the region enclosed by the dotted pink line in (**d**).

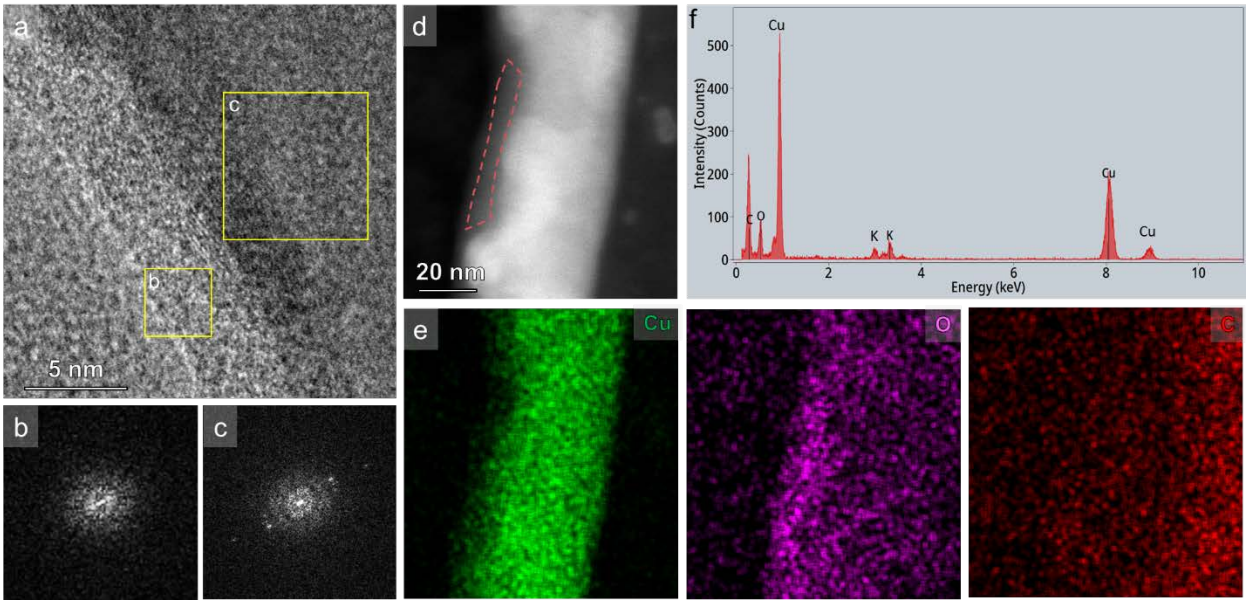

Supplementary Fig. 11 | The characterization of activated copper nanowires by cryo-TEM techniques. (Activation condition: -1.1 V VS. RHE, 60 min) a, HRTEM images of activated nanowires reveal that their structure consists of two distinct parts. **b**, The FFT of square B in Figure A indicates that it possesses an amorphous structure. **c**, The FFT of square C in Figure A indicates that it possesses a crystal structure. **d**, HAADF image and (**e**) EDX mapping show the elemental composition. **f**, The EDX spectrum extracted from the region enclosed by the dotted pink line in (**d**).

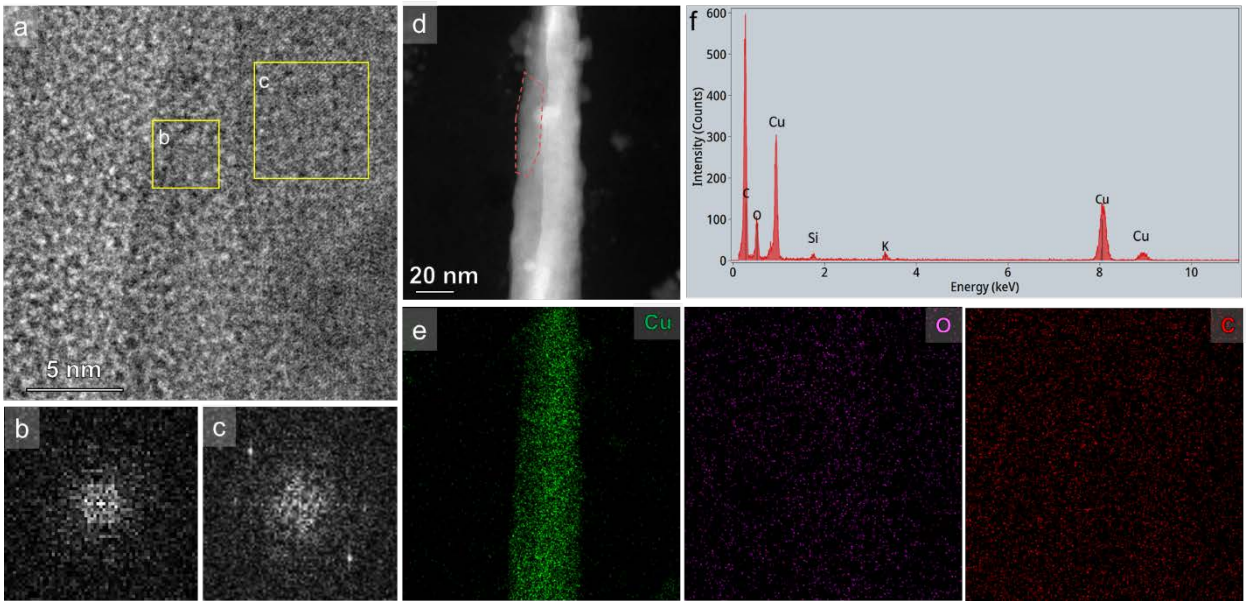

Supplementary Fig. 12 | The characterization of activated copper nanowires by cryo-TEM techniques. (Activation condition: -0.9 V VS. RHE, 30 min) a, HRTEM images of activated nanowires reveal that their structure consists of two distinct parts. **b**, The FFT of square B in (**a**) indicates that it possesses an amorphous structure. **c**, The FFT of square C in (**a**) indicates that it possesses a crystal structure. **d**, HAADF image and (**e**) EDX mapping show the elemental composition. **f**, The EDX spectrum extracted from the region enclosed by the dotted pink line in (**d**).

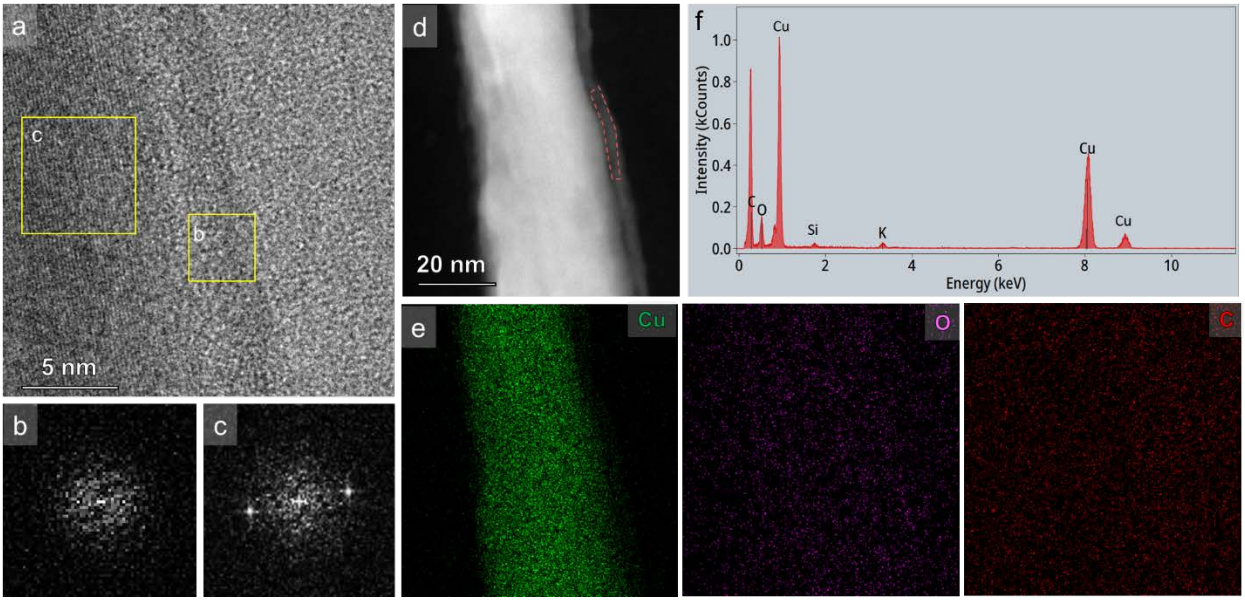

Supplementary Fig. 13 | The characterization of activated copper nanowires by cryo-TEM techniques. (Activation condition: -0.9 V VS. RHE, 60 min) a, HRTEM images of activated nanowires reveal that their structure consists of two distinct parts. **b**, The FFT of square B in (**a**) indicates that it possesses an amorphous structure. **c**, The FFT of square C in (**a**) indicates that it possesses a crystal structure. **d**, HAADF image and (**e**) EDX mapping show the elemental composition. **f**, The EDX spectrum extracted from the region enclosed by the dotted pink line in (**d**).

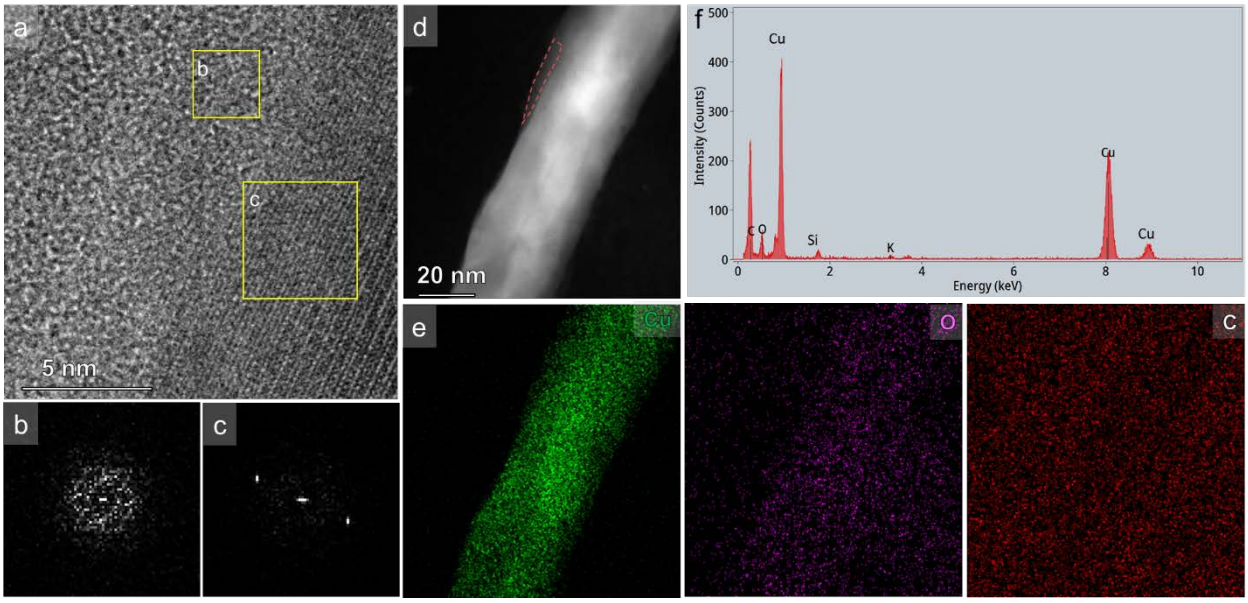

Supplementary Fig. 14 | The characterization of activated copper nanowires by cryo-TEM techniques. (Activation condition: -0.7 V VS. RHE, 30 min) a, HRTEM images of activated nanowires reveal that their structure consists of two distinct parts. **b**, The FFT of square B in (**a**) indicates that it possesses an amorphous structure. **c**, The FFT of square C in (**a**) indicates that it possesses a crystal structure. **d**, HAADF image and (**e**) EDX mapping show the elemental composition. **f**, The EDX spectrum extracted from the region enclosed by the dotted pink line in (**d**).

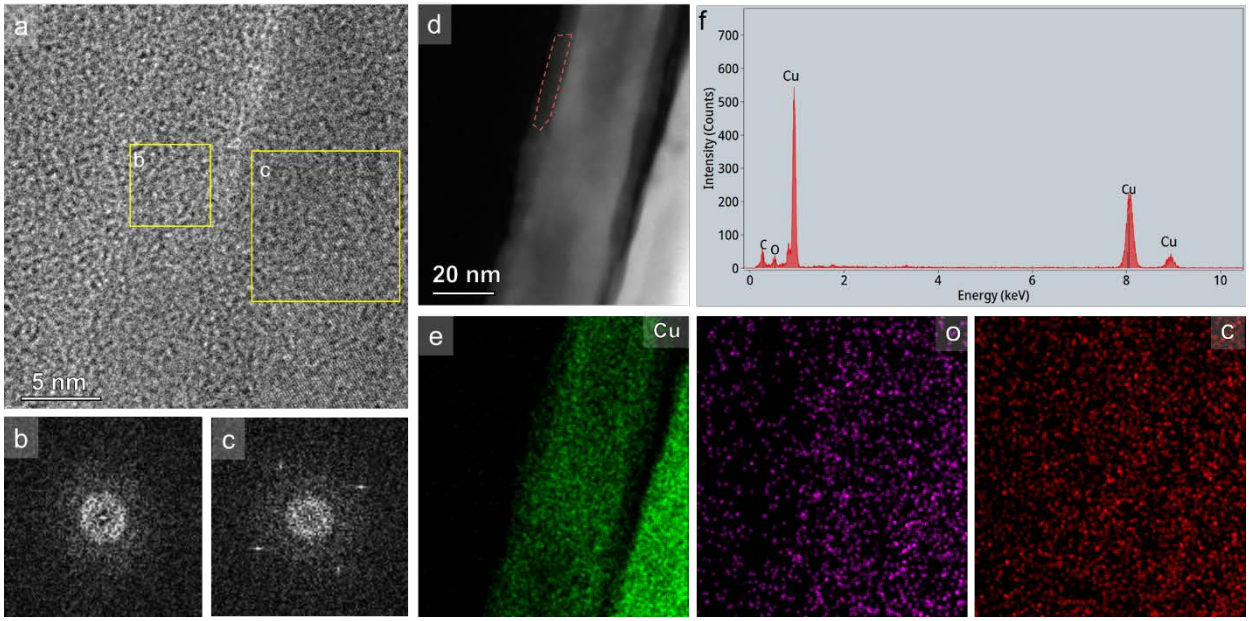

Supplementary Fig. 15 | The characterization of activated copper nanowires by cryo-TEM techniques. (Activation condition: -0.7 V VS. RHE, 60 min) a, HRTEM images of activated nanowires reveal that their structure consists of two distinct parts. **b**, The FFT of square B in (**a**) indicates that it possesses an amorphous structure. **c**, The FFT of square C in (**a**) indicates that it possesses a crystal structure. **d**, HAADF image and (**e**) EDX mapping show the elemental composition. **f**, The EDX spectrum extracted from the region enclosed by the dotted pink line in (**d**).

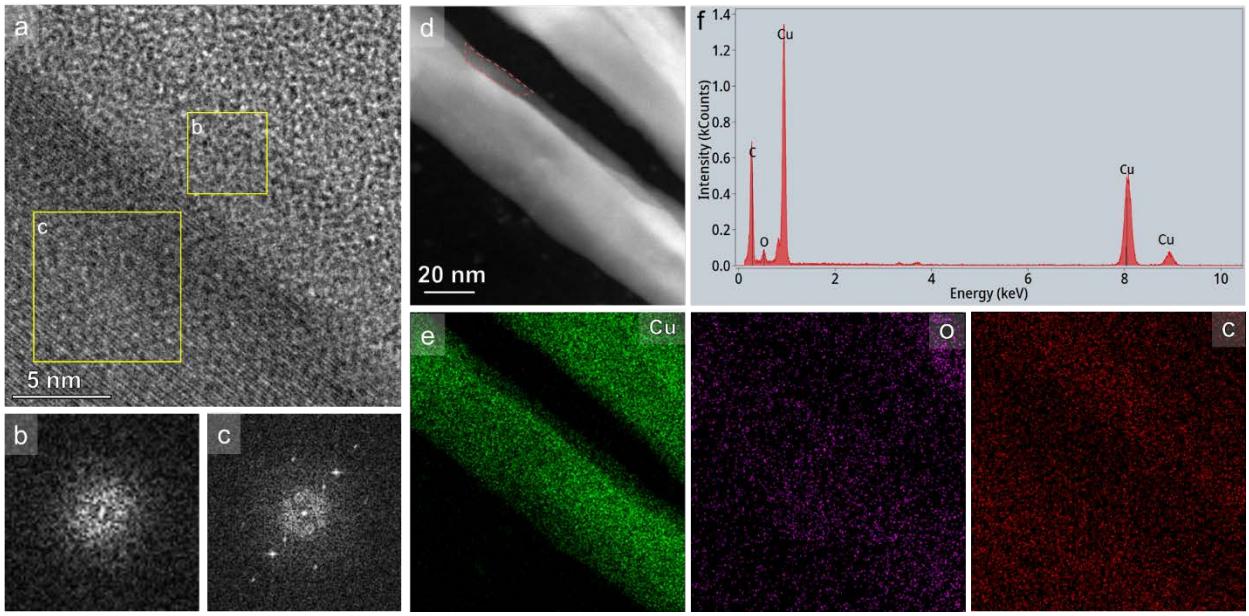

Supplementary Fig. 16 | The characterization of activated copper nanowires by cryo-TEM techniques. (Activation condition: -0.5 V VS. RHE, 30 min) a, HRTEM images of activated nanowires reveal that their structure consists of two distinct parts. **b**, The FFT of square B in (**a**) indicates that it possesses an amorphous structure. **c**, The FFT of square C in (**a**) indicates that it possesses a crystal structure. **d**, HAADF image and (**e**) EDX mapping show the elemental composition. **f**, The EDX spectrum extracted from the region enclosed by the dotted pink line in (**d**).

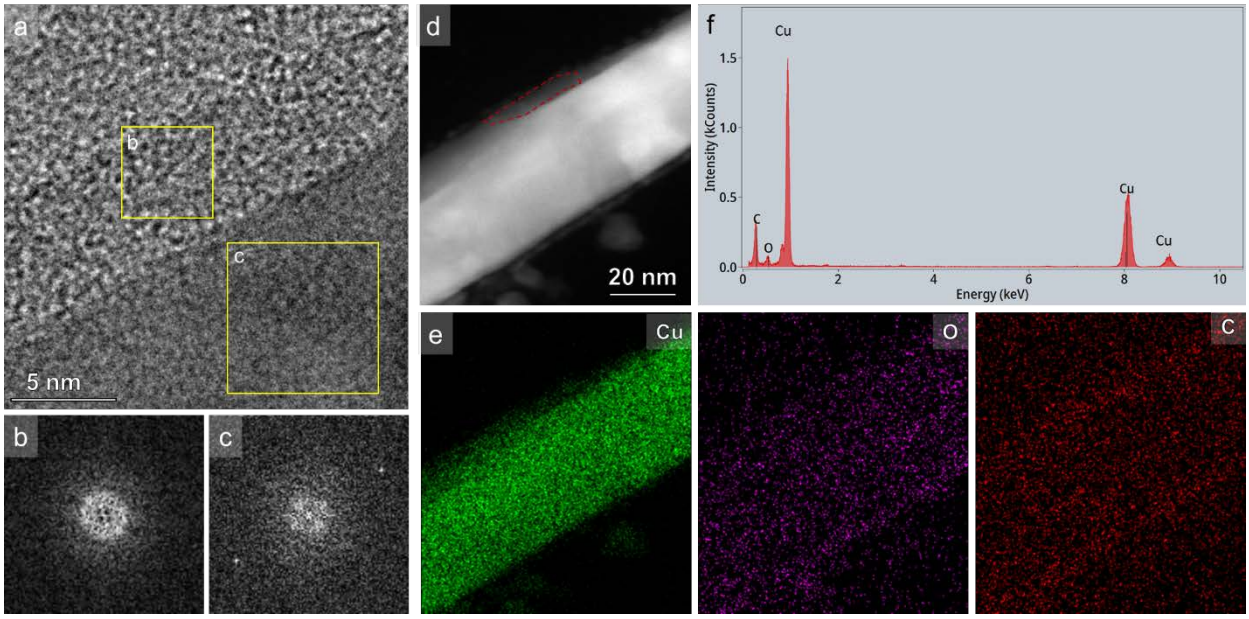

Supplementary Fig. 17 | The characterization of activated copper nanowires by cryo-TEM techniques. (Activation condition: -0.5 V VS. RHE, 60 min) a, HRTEM images of activated nanowires reveal that their structure consists of two distinct parts. **b**, The FFT of square B in (**a**) indicates that it possesses an amorphous structure. **c**, The FFT of square C in (**a**) indicates that it possesses a crystal structure. **d**, HAADF image and (**e**) EDX mapping show the elemental composition. **f**, The EDX spectrum extracted from the region enclosed by the dotted pink line in (**d**).

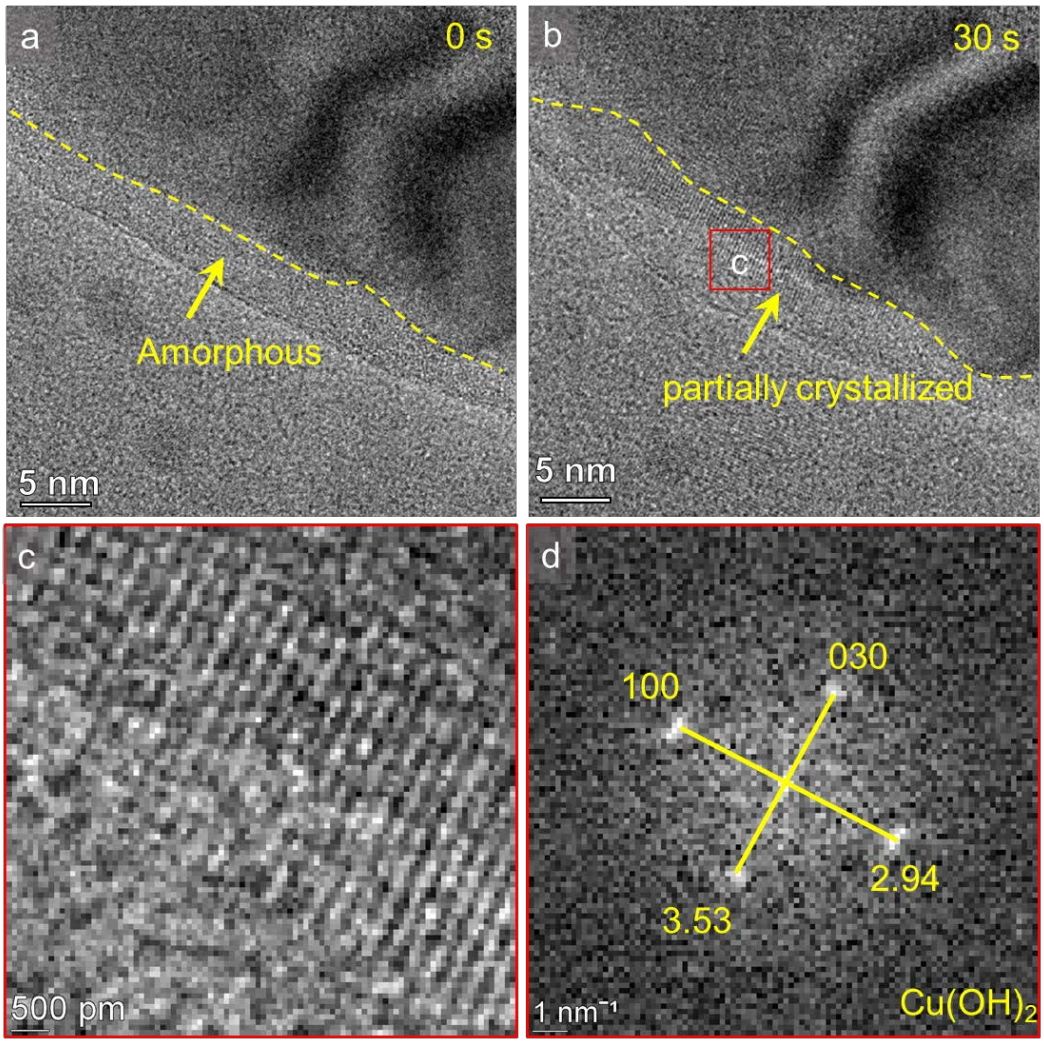

Supplementary Fig. 18 | Electron beam irradiation can crystallize the amorphous layer into $Cu(OH)_2$ after the removal of biasing. **a**, TEM image of an activated Cu nanowire, where the yellow arrow highlights the location of the amorphous layer. **b**, Upon removal of the bias voltage, the amorphous phase partially transformed into crystalline copper hydroxide following 30 seconds of electron beam irradiation. **c**, HRTEM image of $Cu(OH)_2$ captured within the red square area of panel (**b**). **d**, The corresponding FFT pattern for panel (c).

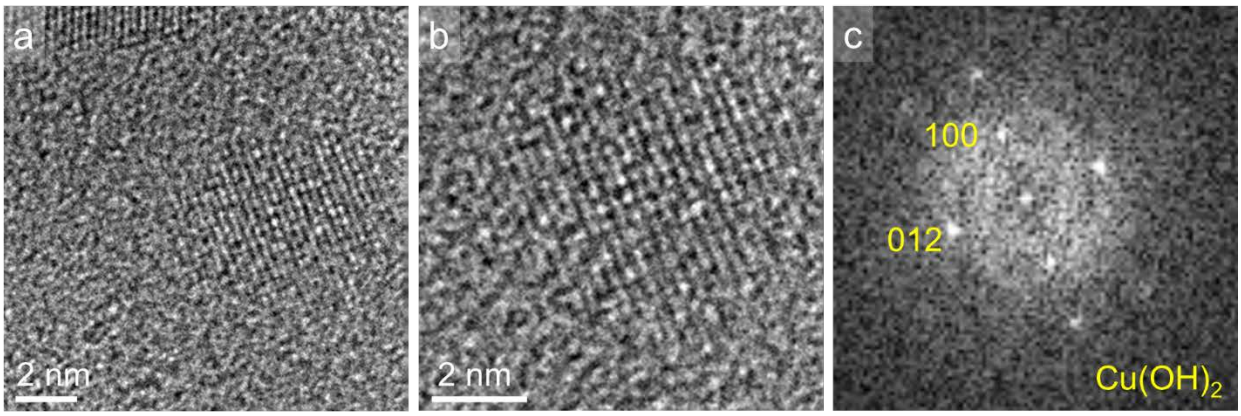

Supplementary Fig. 19 | Characterization of particles formed within the amorphous layer. **a**, TEM image shows a crystal particle formed in the amorphous layer. **b**, HRTEM image of the formed particle. **c**, The corresponding FFT pattern indicates the particle is single crystal $Cu(OH)_2$.

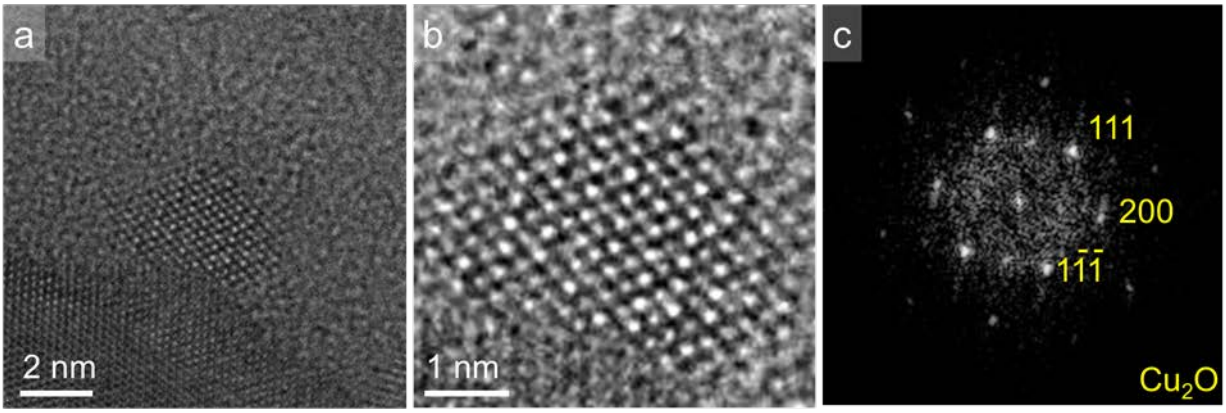

Supplementary Fig. 20 | Characterization of particles formed at the crystal Cu-amorphous interface. a, TEM image shows a crystal particle formed at the crystal Cu-amorphous interface. **b**, HRTEM image of the formed particle. **c**, The corresponding FFT pattern indicates the particle is single crystal Cu_2O.

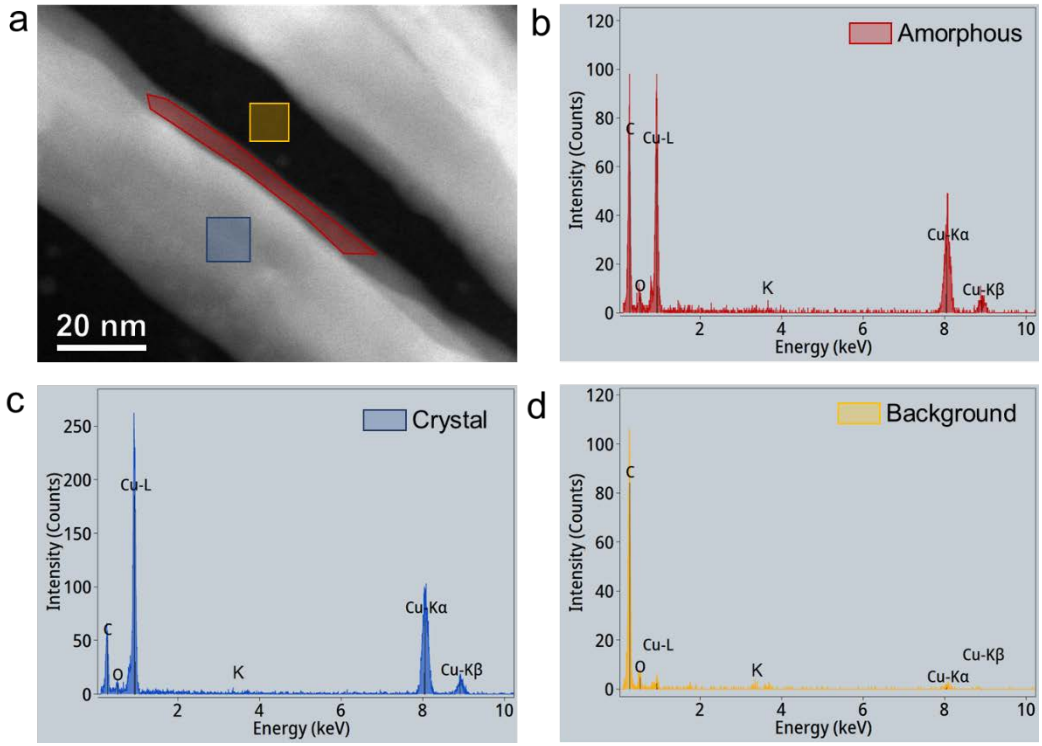

Supplementary Fig. 21 | EDX spectra of various regions within an activated nanowire. **a**, HAADF image of an activated Cu nanowire, where different colors indicate the regions where EDX spectra were acquired. **b**, EDX spectrum of the amorphous region. **c**, EDX spectrum of the crystal region. **d**, EDX spectrum of the background region.

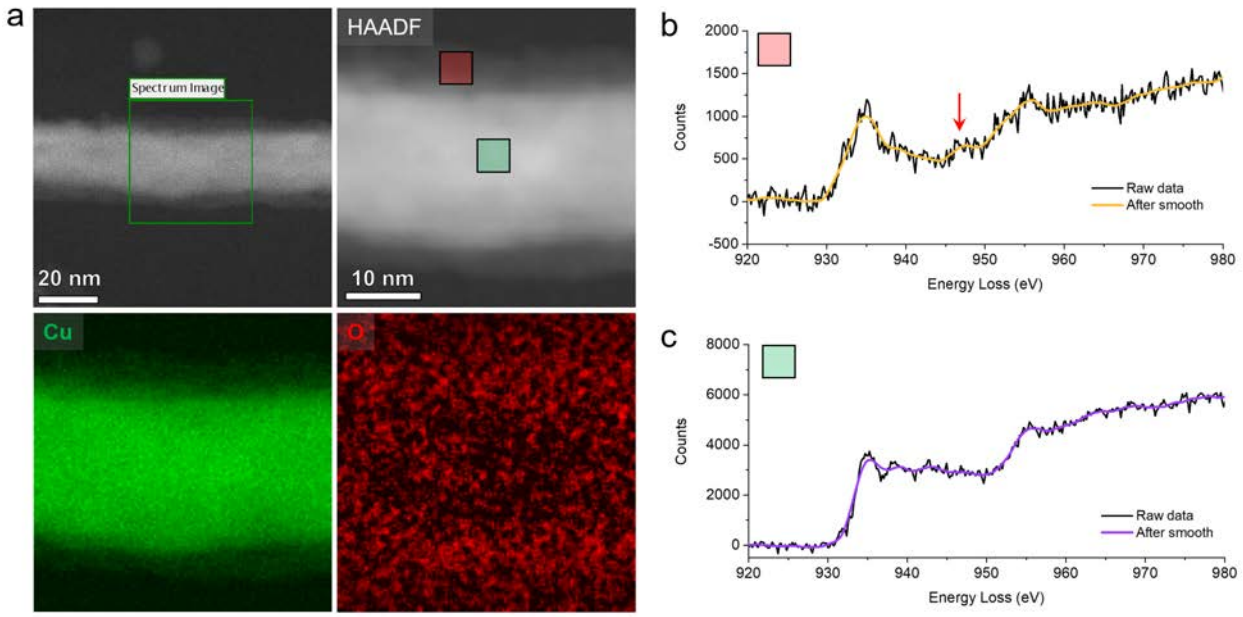

Supplementary Fig. 22 | EELS characterization of an activated nanowire. a, HAADF image and the corresponding EELS mapping of an activated Cu nanowire, where different color squares indicate the regions where EELS spectra were acquired. **b**, EELS spectrum of the amorphous region. **c**, EELS spectrum of the crystal region.

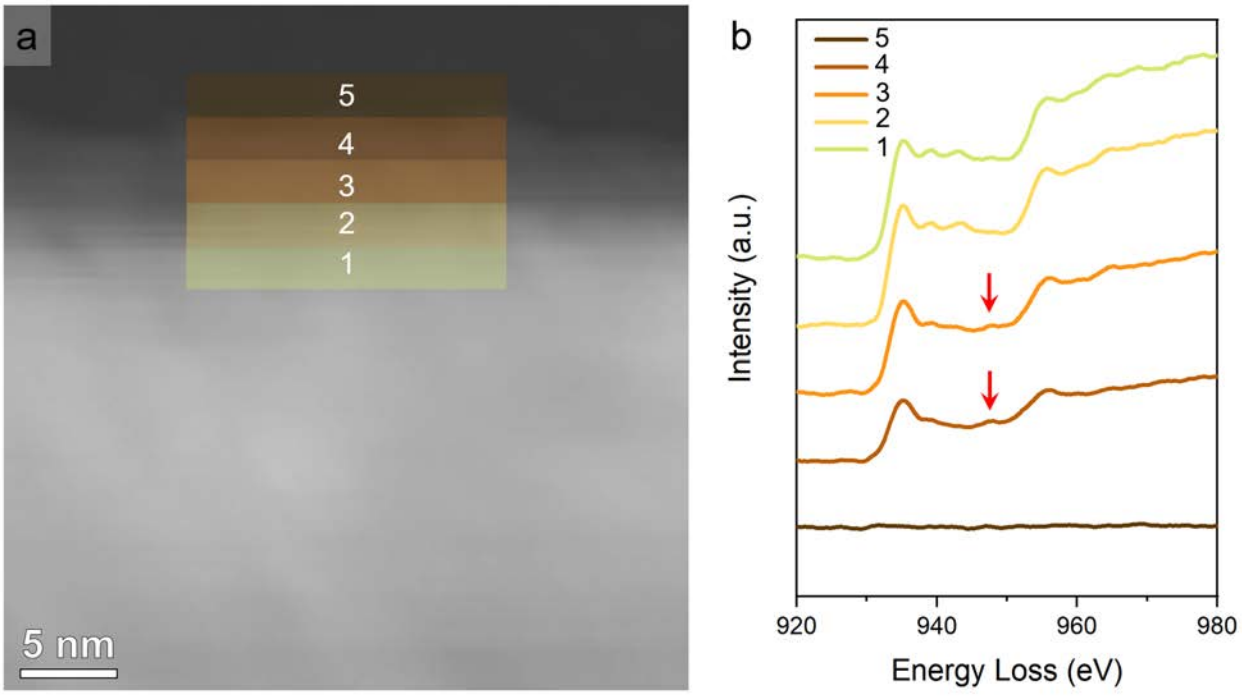

Supplementary Fig. 23 | EELS characterization near amorphous and crystalline interfaces. **a**, HAADF image of an amorphous-crystal interface in an activated Cu nanowire, where different color squares indicate the regions where EELS spectra were acquired. **b**, Analysis of the EELS spectra from distinct regions reveals that the amorphous section contains Cu^{+} ions, while the crystalline portion is predominantly comprised of zero-valent copper. Furthermore, the background exhibits minimal copper signal.

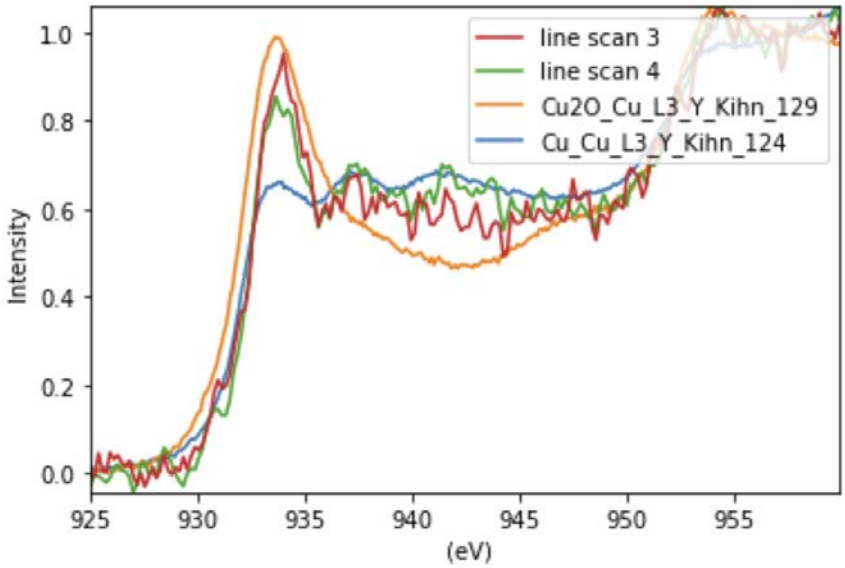

Supplementary Fig. 24 | Experimental EELS spectra and reference spectra after preprocessing. Line scan 3 and line scan 4 are two EELS spectra obtained by performing a line scan in the amorphous region, with scan 4 being closer to the interface between amorphous and crystalline copper. The orange and blue spectra are standard reference spectra obtained from the literature.

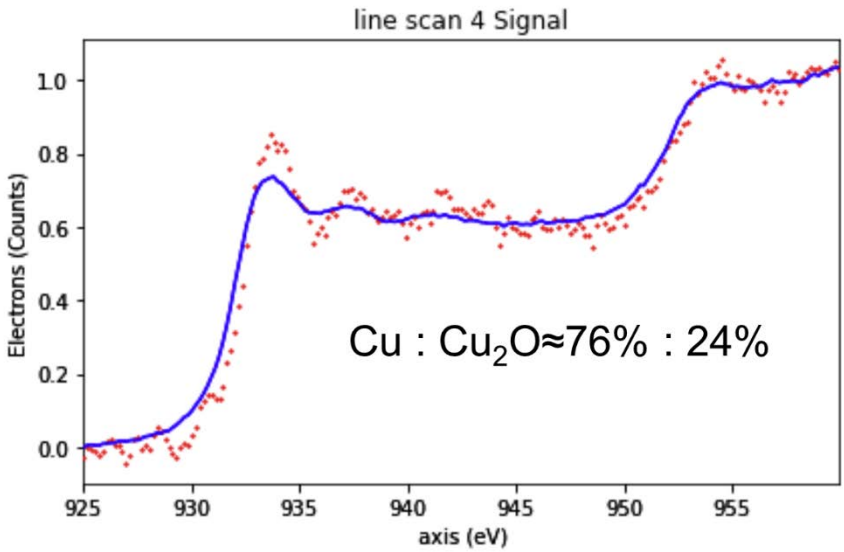

Supplementary Fig. 25 | Experimental EELS spectrum and the linear combination of 76% Cu and 24% Cu_2O reference spectrum.

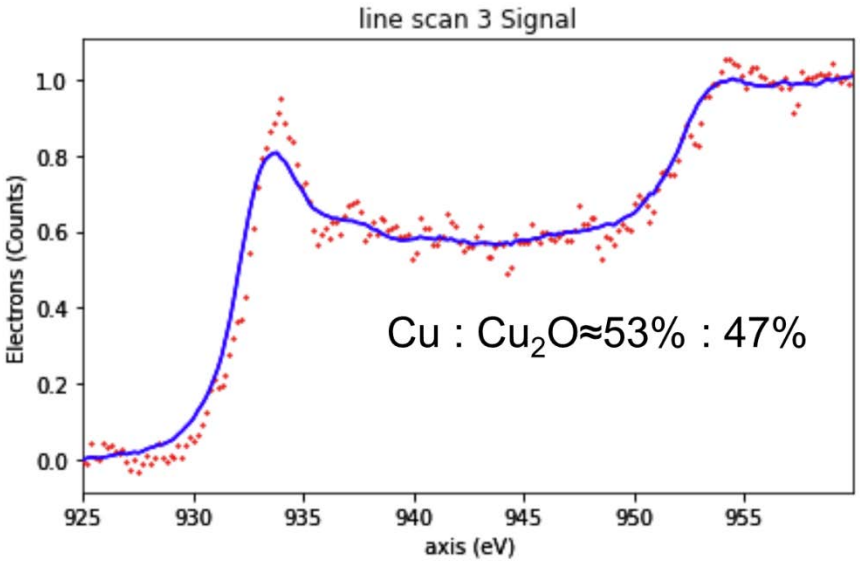

Supplementary Fig. 26 | Experimental EELS spectrum and the linear combination of 53% Cu and 47% Cu_2O reference spectrum.

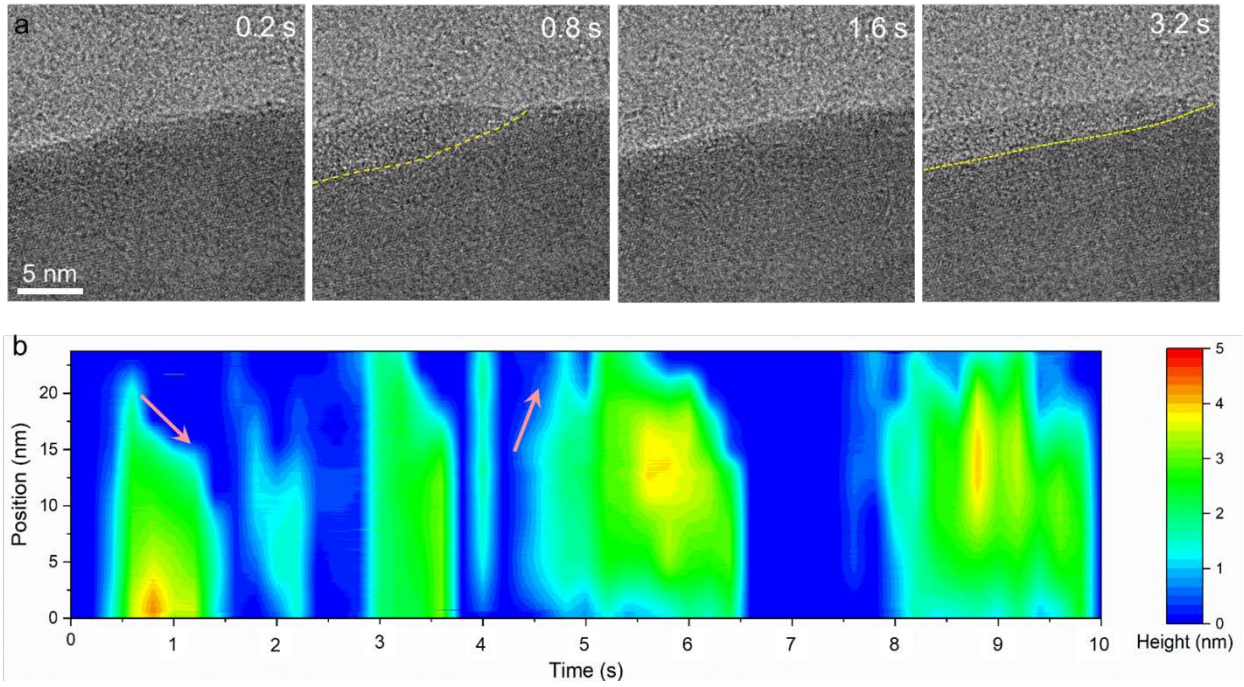

Supplementary Fig. 27 | The raw TEM images from Figure 2A and the dynamics of the amorphous layer's fluctuations. a, The raw TEM images of Figure 2A. **b**, The height of the amorphous layer varies over time. The x-axis represents time, while the y-axis represents the position at the bottom of the image. The height of the amorphous layer is measured as the vertical distance between the upper and lower boundaries of the layer and is indicated by color.

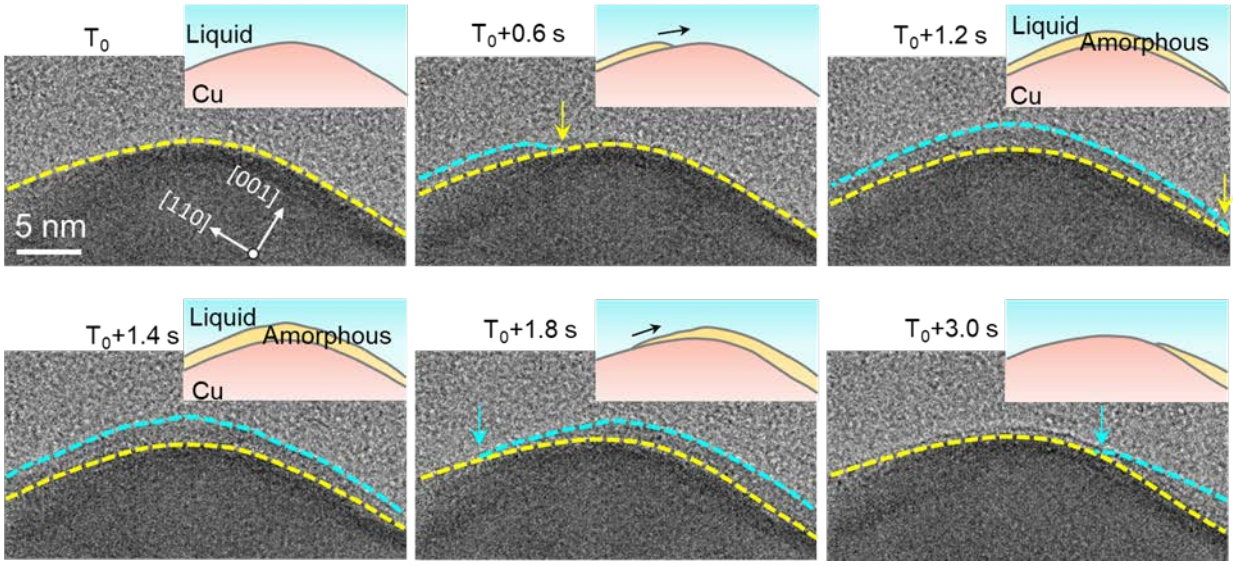

Supplementary Fig. 28 | The raw TEM images of Figure 2b. The yellow dashed line denotes the interface between the crystalline and amorphous regions of the nanowire, or between the amorphous region and the electrolyte. The indigo dashed line indicates the interface between the amorphous region and the electrolyte. In the schematic diagram, the red, yellow, and blue sections represent crystalline copper, the amorphous phase, and the electrolyte, respectively. It is evident from the diagram that the amorphous phase is shifting towards the right. The yellow arrow indicates the leading edge of the amorphous layer movement, while the blue arrow shows the trailing edge of the movement of the amorphous layer.

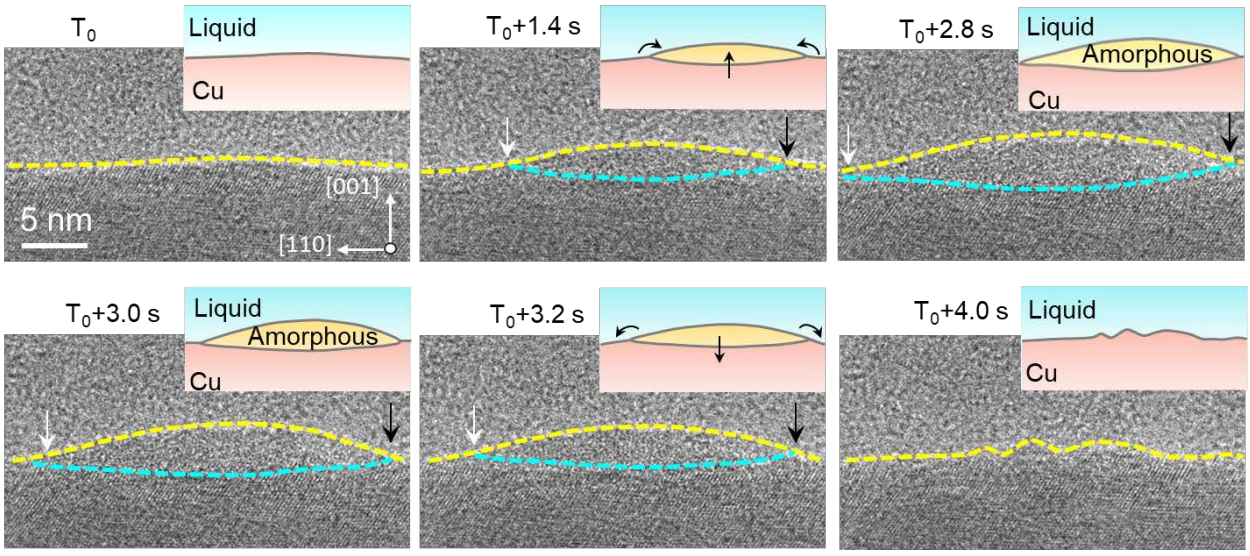

Supplementary Fig. 29 | The raw TEM images of Figure 2C. The yellow dashed line denotes the interface between the nanowire and electrolyte. The indigo dashed line indicates the interface between the amorphous region and the crystal region. In the schematic diagram, the red, yellow, and blue sections represent crystalline copper, the amorphous phase, and the electrolyte, respectively. The schematic diagram illustrates that the transformation of crystals into an amorphous phase and back to crystals results in the previously flat surface becoming curved. The white arrow indicates the left edge of the amorphous layer, while the black arrow shows the right edge of the amorphous layer.

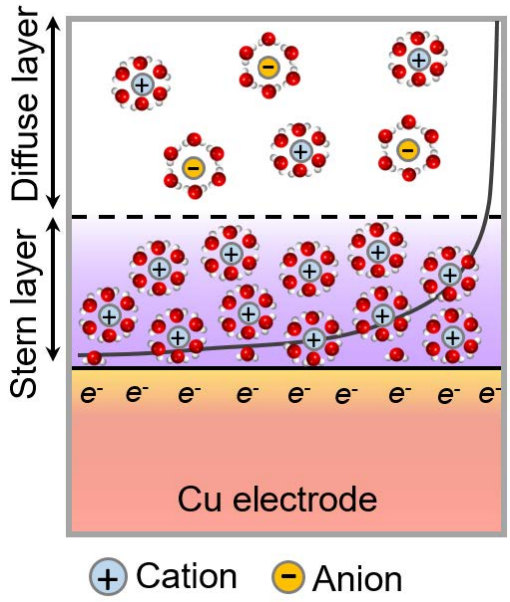

Supplementary Fig. 30 | The electrical double-layer model shows the electron and ion distribution.

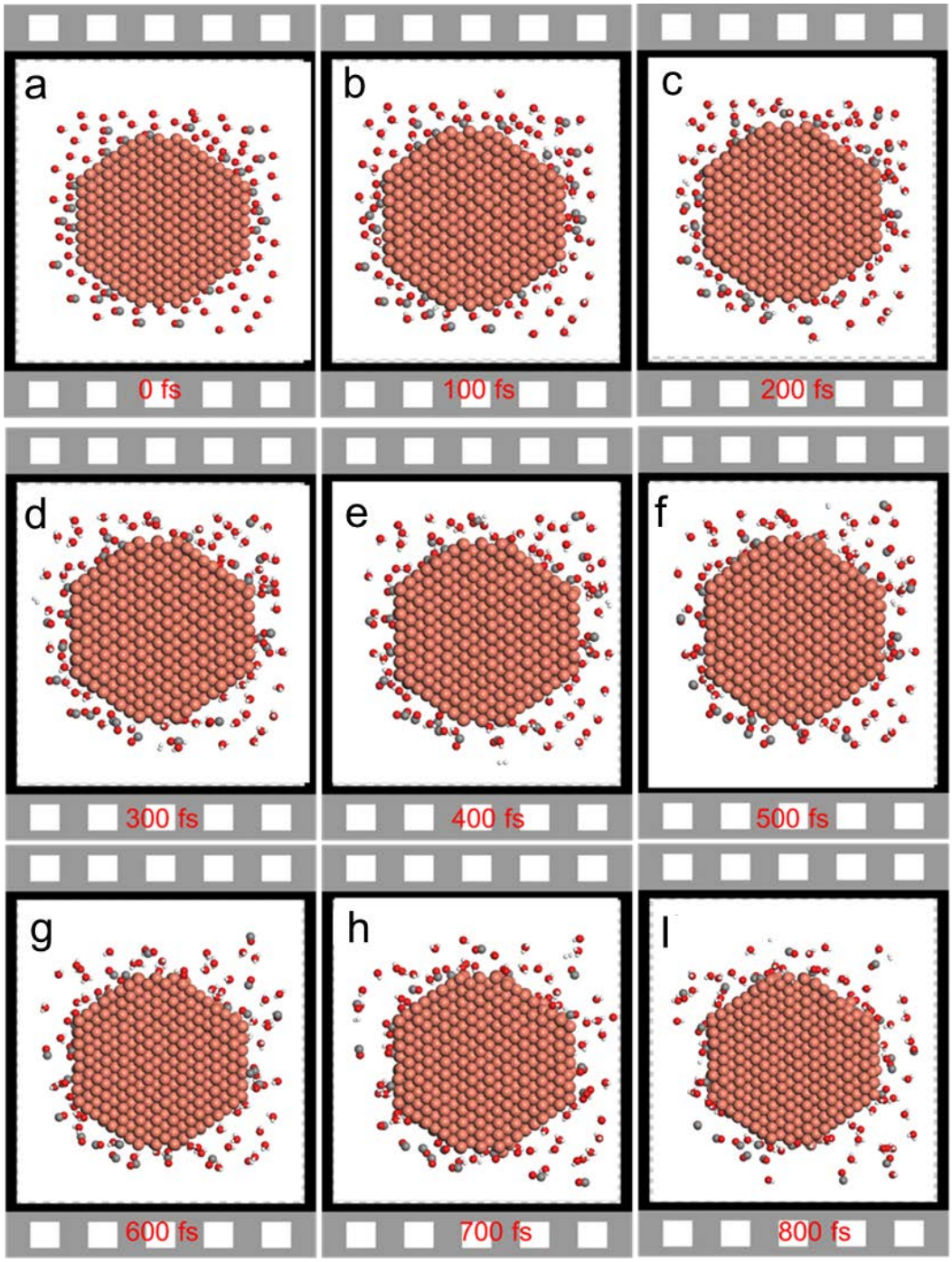

Supplementary Fig. 31 | Snaps of molecular dynamics simulation of Cu nanowire surrounded by CO and H_2O. No doping is applied. The gray, red, white and light red balls represent C, O, H and Cu atoms respectively. Only crossing views of nanowires are shown.

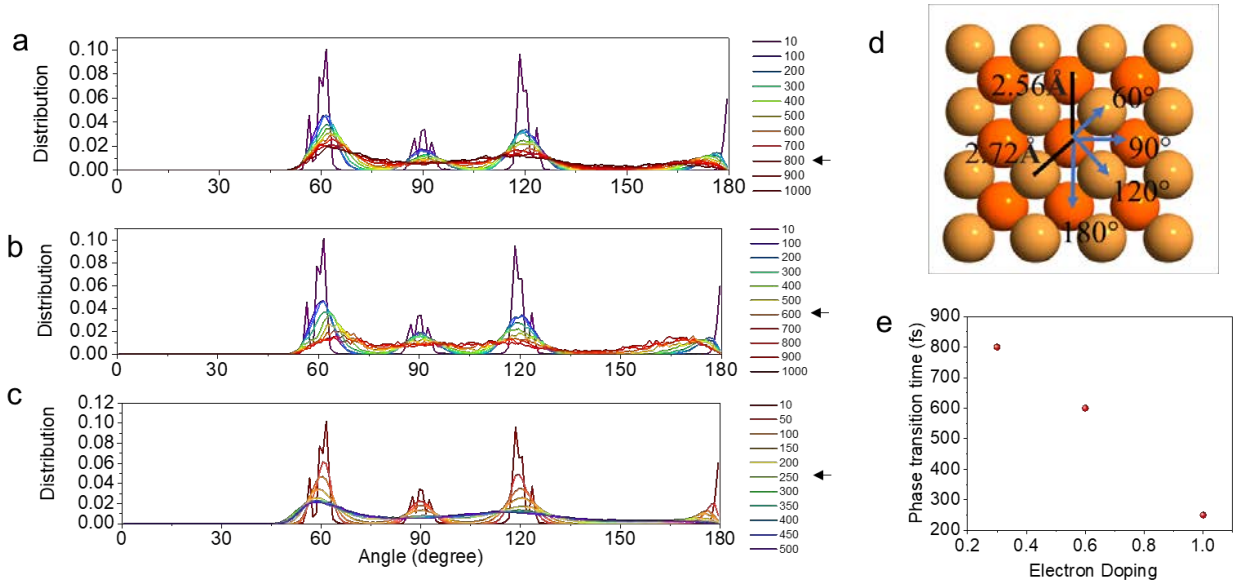

Supplementary Fig. 32 | Analysis of amorphous layer upon doping. a-c, Angular distribution spectrums vary as time when the materials are doped with 0.3, 0.5, 1.0 e/atom. Arrows index the phase transition time. **d**, Illustration of the angular distribution. **e**, Phase transition time as a function of electron doping in a unit of e/atom.

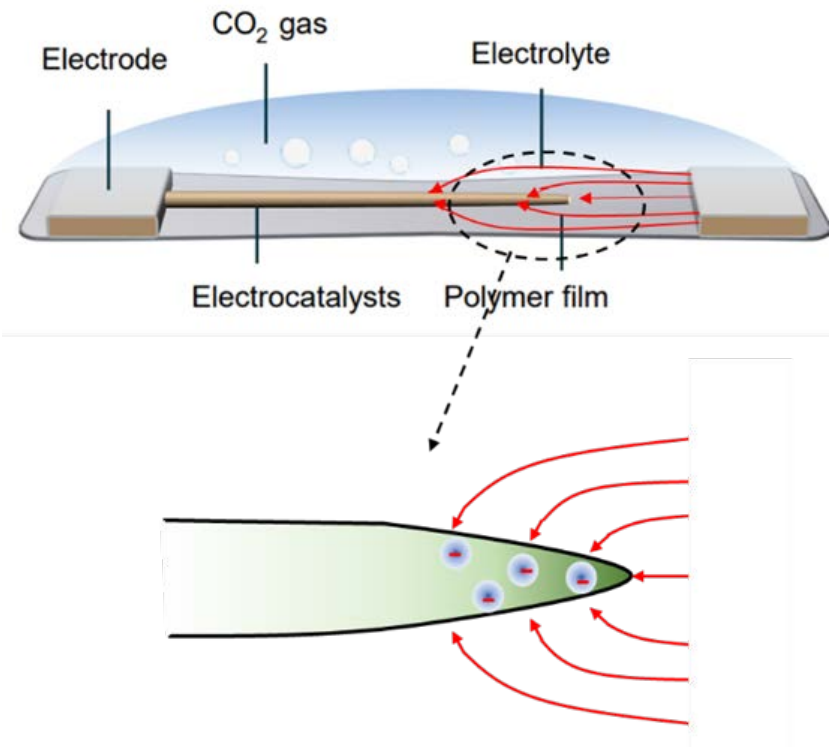

Supplementary Fig. 33 | Illustration of electrode effect. An electrode induces the charge redistribution, especially on the electrode surface.

Supplementary Table 1 | Key EELS spectrum features [7,8].

EELS Spectrum Region	L_3 peak position	L_3/L_2 height ratio
Cu^{2+} : ref. CuO	933.6 eV	1.79
Cu^{1+} : ref. Cu_2O	936.1 eV	0.94
Cu^{0} : ref. Cu	935.5 eV	0.68
Amorphous transition layer	936.3 eV	0.83
Crystal Cu	934.8 eV	0.70

Supplementary Table 2 | Vacancy formation energies at different sites on a crystalline copper surface.

	Terrace	Step edge (single)	Step edge (multiple)	Step edge (mean of multiple)
Model	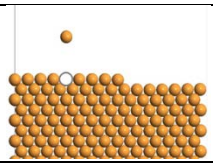	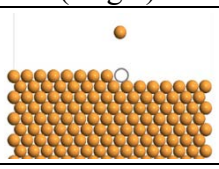	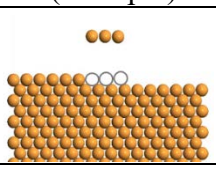	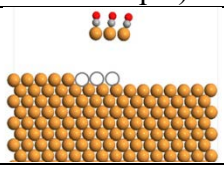
In vacuum	2.791 eV	2.387 eV	4.11 eV	1.37 eV
In solvent (water)	2.914 eV	2.51 eV	4.22 eV	1.41 eV
Doping 1e/atom	0.61 eV	0.58 eV	1.54 eV	0.51eV

Supplementary Video 1.

Formation and fluctuation of a gel-like amorphous interphase on the surface of Cu nanowire during CO_2 electroreduction. The electrolyte is 0.1 M $KHCO_3$ aqueous solution saturated CO_2 gas. The potential is -1.1 V (vs. RHE) and the beam condition is 2360 e/Å^{2}s.

Supplementary Video 2.

The dynamics show the amorphous interphase appearing and disappearing repeatedly, exhibiting fluidity and fluctuation. The beam condition is 2360 e/Å^{2}s

Supplementary Video 3.

The control experiment shows, under the same environment and beam conditions and without biasing, no amorphous interphase formed on the surface of the nanowire. The electrolyte is 0.1 M $KHCO_3$ aqueous solution saturated CO_2 gas. The beam condition is 2360 e/Å^{2}s.

Supplementary Video 4.

A representative example of an amorphous interphase domain diffusion along the crystalline Cu surface. The beam condition is 2360 e/Å^{2}s

Supplementary Video 5.

The formation and phase transformation of an amorphous interphase domain roughens the flat surface of a Cu nanowire. The beam condition is 2360 e/Å^{2}s

Supplementary Video 6.

The crystalline Cu surface covered by the amorphous interphase experiences more severe dissolution of Cu than the bare Cu surface. The electrolyte is 0.1 M $KHCO_3$ aqueous solution saturated CO_2 gas. The potential is -1.1 V (vs. RHE) and the beam condition is 6920 e/Å^{2}s.

Supplementary Video 7.

The Cu atoms are removed along the atomic step edge at the interface between crystal Cu and electrolyte. The beam condition is 6920 e/Å^{2}s.

Supplementary Video 8.

The Cu atoms are removed more dramatically and randomly at the interface between the crystalline Cu and the amorphous. The beam condition is 6920 e/Å^{2}s.

Supplementary Video 9.

Another example of copper atoms being randomly removed at the interface between crystalline Cu and amorphous Cu. Although initially, the atoms located at the atomic step edges were preferentially eliminated, this inclination rapidly diminished, allowing for simultaneous removal of atoms at the terraces and steps. The beam condition is 6920 e/Å^{2}s.

1 Yang, Y. *et al.* Operando studies reveal active Cu nanograins for CO2 electroreduction. *Nature* **614**, 262-269 (2023).
2 Egerton, R., Li, P. & Malac, M. Radiation damage in the TEM and SEM. *Micron* **35**, 399-409 (2004).
3 Nakamura, R., Ishimaru, M., Yasuda, H. & Nakajima, H. Atomic rearrangements in amorphous Al2O3 under electron-beam irradiation. *J. Appl. Phys.* **113**, 064312 (2013).
4 Jenčič, a., Bench, M., Robertson, I. & Kirk, M. Electron-beam-induced crystallization of isolated amorphous regions in Si, Ge, GaP, and GaAs. *J. Appl. Phys.* **78**, 974-982 (1995).
5 Zhang, Q. *et al.* Swap motion–directed twinning of nanocrystals. *Sci. Adv.* **8**, eabp9970 (2022).
6 Jeon, S. *et al.* Reversible disorder-order transitions in atomic crystal nucleation. *Science* **371**, 498-503 (2021).
7 Keast, V., Scott, A., Brydson, R., Williams, D. & Bruley, J. Electron energy-loss near-edge structure-a tool for the investigation of electronic structure on the nanometre scale. *J. Microsc.* **203**, 135-175 (2001).
8 Yang, G. *et al.* Investigation of the oxidation states of Cu additive in colored borosilicate glasses by electron energy loss spectroscopy. *J. Appl. Phys.* **116**, 223707 (2014).